



# Benchmarking the PreSPEC@GSI experiment for Coulex-multipolarimetry on the $\pi(p_{3/2}) \rightarrow \pi(p_{1/2})$ spin-flip transition in $^{85}\text{Br}$

P. Napiřalla<sup>1,2,a</sup> , M. Lettmann<sup>1</sup>, C. Stahl<sup>1</sup>, G. Rainovski<sup>3</sup>, N. Pietralla<sup>1</sup>, S. Afara<sup>4</sup>, F. Ameil<sup>2</sup>, T. Arici<sup>2</sup>, S. Aydin<sup>5</sup>, D. Barrientos<sup>6</sup>, P. Bednarczyk<sup>7</sup>, M. A. Bentley<sup>8</sup>, G. Benzoni<sup>9</sup>, B. Birkenbach<sup>10</sup>, A. Blazhev<sup>10</sup>, A. J. Boston<sup>11</sup>, P. Boutachkov<sup>1,2</sup>, A. Bracco<sup>9</sup>, B. Bruyneel<sup>12</sup>, E. Clément<sup>13</sup>, M. L. Cortés<sup>1,2,14</sup>, F. C. L. Crespi<sup>9</sup>, D. M. Cullen<sup>15</sup>, D. Curien<sup>16</sup>, P. Déesquelles<sup>17</sup>, F. Didierjean<sup>16</sup>, C. Domingo-Pardo<sup>18</sup>, G. Duchêne<sup>16</sup>, J. Eberth<sup>10</sup>, H. Egger<sup>19</sup>, C. Fahlander<sup>20</sup>, J. Gerl<sup>2</sup>, K. A. Gladnishki<sup>3</sup>, P. Golubev<sup>20</sup>, V. González<sup>21</sup>, M. Górška<sup>2</sup>, A. Gottardo<sup>22</sup>, L. Grassi<sup>23</sup>, T. Habermann<sup>2</sup>, L. J. Harkness-Brennan<sup>11</sup>, H. Hess<sup>10</sup>, D. G. Jenkins<sup>8</sup>, P. R. John<sup>1</sup>, J. Jolie<sup>10</sup>, D. S. Judson<sup>11</sup>, I. Kojouharov<sup>2</sup>, W. Korten<sup>12</sup>, M. Labiche<sup>24</sup>, N. Lalović<sup>20</sup>, C. Lizarazo<sup>1,2</sup>, C. Louchart-Henning<sup>1,2</sup>, A. Maj<sup>7</sup>, R. Menegazzo<sup>25</sup>, D. Mengoni<sup>23</sup>, E. Merchan<sup>1,2</sup>, B. Million<sup>9</sup>, O. Möller<sup>1</sup>, T. Möller<sup>1</sup>, K. Moschner<sup>10</sup>, V. Modamio<sup>14</sup>, D. Napoli<sup>14</sup>, B. S. Nara Singh<sup>26,27</sup>, Zs. Podolyák<sup>28</sup>, S. Pietri<sup>2</sup>, D. Ralet<sup>1,2,22</sup>, M. Reese<sup>2</sup>, P. Reiter<sup>10</sup>, D. Rudolph<sup>20</sup>, E. Sanchis<sup>21</sup>, L. G. Sarmiento<sup>20</sup>, H. Schaffner<sup>2</sup>, J. Simpson<sup>24</sup>, P. P. Singh<sup>2</sup>, J. J. Valiente-Dobón<sup>14</sup>, V. Werner<sup>1</sup>, O. Wieland<sup>9</sup>

- <sup>1</sup> Institut für Kernphysik, Technische Universität Darmstadt, Schlossgartenstr. 9, 64289 Darmstadt, Germany
- <sup>2</sup> GSI Helmholtzzentrum für Schwerionenforschung GmbH, Planckstr. 1, 64291 Darmstadt, Germany
- <sup>3</sup> Faculty of Physics, St. Kliment Ohridski University of Sofia, 5 James Bourchier Blvd., 1164 Sofia, Bulgaria
- <sup>4</sup> King Saud University, P. O. BOX 2454, Riyadh 11451, Saudi Arabia
- <sup>5</sup> Bahçe Saray Mahallesi, Aksaray University, Aksaray-Adana Yolu, Sağlık/Aksaray, Merkez/Aksaray, 68100 Aksaray, Turkey
- <sup>6</sup> CERN, CH-1211 Geneva 23, Geneva, Switzerland
- <sup>7</sup> The Henryk Niewodniczański Institute of Nuclear Physics, Polish Academy of Sciences, ul. Radzikowskiego 152, 31-342 Kraków, Poland
- <sup>8</sup> Department of Physics, University of York, Heslington YO10 5DD, UK
- <sup>9</sup> Istituto Nazionale di Fisica Nucleare, Sezione di Milano, Via Celoria 16, 20133 Milan, Italy
- <sup>10</sup> Institut für Kernphysik, Universität zu Köln, Zùlpicher Str. 77, 50937 Köln, Germany
- <sup>11</sup> Oliver Lodge Laboratory, The University of Liverpool, Liverpool L69 7ZE, UK
- <sup>12</sup> Irfu, CEA, Université Paris-Saclay, 91191 Gif-sur-Yvette, France
- <sup>13</sup> Grand Accélérateur National d'Ions Lourds–GANIL, CEA/DSAM and CNRS/IN2P3, BP 55027, 14076 Caen Cedex 05, France
- <sup>14</sup> Laboratori Nazionali di Legnaro, Istituto Nazionale di Fisica Nucleare, Viale dell'Università, 2, 35020 Legnaro, PD, Italy
- <sup>15</sup> Nuclear Physics Group, Schuster Laboratory, University of Manchester, Manchester M13 9PL, UK
- <sup>16</sup> Université de Strasbourg, CNRS, IPHC UMR 7178, 67000 Strasbourg, France
- <sup>17</sup> CSNSM, Université Paris-Sud and CNRS-IN2P3, Université Paris-Saclay, Bat 104, 91405 Orsay Campus, France
- <sup>18</sup> Instituto de Física Corpuscular, CSIC-Universidad de Valencia, 46071 Valencia, Spain
- <sup>19</sup> AG Numerik und Wissenschaftliches Rechnen, Technische Universität Darmstadt, Dolivostr. 15, 64293 Darmstadt, Germany
- <sup>20</sup> Department of Physics, Lund University, 22100 Lund, Sweden
- <sup>21</sup> Departamento de Ingeniería Electrónica, Universidad de Valencia, Burjassot, Valencia, Spain
- <sup>22</sup> Institut de Physique Nucléaire, IN2P3-CNRS, Université Paris-Sud, Université Paris-Saclay, 91405 Orsay, France
- <sup>23</sup> Dipartimento di Fisica e Astronomia “Galileo Galilei”, Università di Padova and INFN, Sezione di Padova, Padua 35131, Italy
- <sup>24</sup> STFC Daresbury Laboratory, Daresbury, Warrington WA4 4AD, UK
- <sup>25</sup> Istituto Nazionale di Fisica Nucleare, Sezione di Padova, 35131 Padua, Italy
- <sup>26</sup> School of Physics and Astronomy, The University of Manchester, Schuster Building, Manchester M13 9PL, UK
- <sup>27</sup> School of Engineering and Computing, University of the West of Scotland, Paisley PA1 2BE, UK
- <sup>28</sup> Department of Physics, University of Surrey, Guildford GU2 7XH, UK

Received: 19 January 2020 / Accepted: 22 April 2020 / Published online: 25 May 2020  
© Società Italiana di Fisica and Springer-Verlag GmbH Germany, part of Springer Nature 2020  
Communicated by Calin Alexandru Ur

**Abstract** A first performance test of the Coulomb excitation multipolarimetry (*Coulex-multipolarimetry*) method

is presented. It is based on a  $^{85}\text{Br} \pi p_{3/2} \rightarrow \pi p_{1/2}$  spin-flip experiment performed as part of the PreSPEC-AGATA campaign at the GSI Helmholtzzentrum für Schwerionen-

<sup>a</sup> e-mail: [pnapiřalla@ikp.tu-darmstadt.de](mailto:pnapiřalla@ikp.tu-darmstadt.de) (corresponding author)

forschung (GSI). Via determination of background levels around the expected  $^{85}\text{Br}$  excitations as well as measured  $^{197}\text{Au}$  excitations, an upper limit for the  $M1$  transition strength of the  $1/2_1^- \rightarrow 3/2_{\text{g.s.}}^-$  transition in  $^{85}\text{Br}$  and a lower beam time limit for upcoming experimental campaigns utilizing *Coulex-multipolarimetry* have been inferred. The impact of the use of AGATA in its anticipated  $1\pi$  configuration on these estimates is deduced via *Geant4* simulations.

## 1 Introduction

The identification of single-particle states in even-odd nuclei via the measurement of spin-flip transitions is an experimental tool to investigate nuclear shell evolution in the vicinity of closed shells. These are transitions of a single nucleon between a  $j_> = \ell + 1/2$  and a  $j_< = \ell - 1/2$  state, i.e. between spin-orbit partners and exhibit some of the largest known  $M1$  transition strengths of  $\sim 1 \mu_N^2$ . These large transition strengths serve as a unique signature for spin-flip transitions, giving insight into the role of specific orbitals in nuclear eigenstates.

In order to investigate nuclear shell evolution towards the doubly-magic nucleus  $^{78}\text{Ni}$  [1], many experimental [2–4] and theoretical studies [3, 5, 6] have been performed in the vicinity of the nickel isotopic chain towards  $^{78}\text{Ni}$ . These studies suggest severe changes in single-particle energies, interpreted as being caused by the tensor-force [5, 6] as a function of the filling of the  $\nu g_{9/2}$  shell. In the isotonic chain  $N = 50$ , the  $1/2_1^- \rightarrow 3/2_{\text{g.s.}}^-$  transition at 845 keV in  $^{87}\text{Rb}$  with an  $M1$  transition strength of  $0.64_{-5}^{+8} \mu_N^2$  [7] was identified as the main fragment of the  $\pi p_{1/2} \rightarrow \pi p_{3/2}$  single-particle transition. In the neutron-rich even-odd nucleus  $^{85}\text{Br}$ , the  $1/2_1^-$  state at 1191 keV is considered to be the most likely candidate for a  $\pi p_{3/2} \rightarrow \pi p_{1/2}$  single-particle excitation, which would correspond to a sudden increase in excitation energy of the  $\pi p_{1/2}$  orbital from  $^{87}\text{Rb}$  to  $^{85}\text{Br}$ .

To this end, the simultaneous measurement of two crucial quantities, the level lifetime and the degree of  $M1$  character of its decay transition are required. The spin quantum number  $j = 1/2$  of the upper level prevents the measurement of the  $E2/M1$  multipole mixing ratio with the traditional method of angular correlations of the  $1/2_1^- \rightarrow 3/2_{\text{g.s.}}^-$   $\gamma$ -decay intensity due to isotropically emitted  $\gamma$  rays. Hence, a novel experimental technique, called *Coulex-multipolarimetry* [8] was proposed. It was designed such that a direct measurement of the  $E2/M1$  multipole mixing ratio  $\delta$  and the lifetime could be accessed via comparison of different experimental  $\gamma$ -ray yields in Coulomb-excitation reactions. An experiment for benchmarking the potential of the method for future high-intensity relativistic ion beams was performed during the PreSPEC campaign [9] at GSI, utilizing the FRagment

Separator (FRS) [10], the Lund–York–Cologne CALorimeter (LYCCA) [11], the Advanced GAMMA Tracking Array (AGATA) [12] and the High Energy deteCTOR (HECTOR) [13]. The method employs an unconventional target setup, utilizing two consecutive thick gold targets instead of one which allows for two different beam energies in a single setup.

In the following, a brief description of the experimental method and setup, expected yields of target- to beam-like excitations as well as data analysis methods are presented. The measured  $\gamma$ -ray spectra are presented and the achievable performance of the setup is discussed. Potential areas for improvements based on different geometrical setups of AGATA accessed via simulations as well as the impact of  $\gamma$ -ray tracking methods are shown. Estimates on necessary beam time for future experiments employing *Coulex-multipolarimetry* are given.

## 2 Experiment

### 2.1 Coulex-multipolarimetry

The *Coulex-multipolarimetry* was tested for the first time in order to measure the  $M1$  transition strength of the potential spin-flip in  $^{85}\text{Br}$ . Since the ratio of Coulomb excitation cross sections between  $M1$  and  $E2$  excitations scales with the incident beam velocity with  $\beta^2$  [14], the  $E2/M1$  multipole-mixing ratio  $\delta$  is accessible via measurement and comparison of Coulomb-excitation  $\gamma$ -ray yields for two different well chosen incident beam energies. For a sensitive range of multipole mixing ratios, here  $0.01 \lesssim \delta \lesssim 0.1$ , it is possible to access  $\delta$  experimentally via  $\gamma$ -ray yield measurements [8]. To minimize the necessary beam time, the use of two consecutive targets with one incident beam energy instead of a single one with two beam energies was proposed. This approach relies on AGATA's high position resolution for Doppler corrections. Since the energy loss of the beam in matter can be measured or approximated via energy loss calculations, e.g., using ATIMA [15] or LISE++ [16], a second beam energy after the first target is realized, allowing for a measurement of two beam energies with a single incident beam.

### 2.2 Setup

The primary  $^{86}\text{Kr}$  beam extracted from SIS18 at GSI with an incident kinetic energy of 730 MeV/u impinged on a thick  $^9\text{Be}$  target. The produced fragments were mass- and charge-separated by the FRS in such a way that an almost pure neutron-rich  $^{85}\text{Br}$  beam with an energy of 300 MeV/u at an average particle rate of  $4.9 \times 10^4 \text{ s}^{-1}$  has been achieved at the entrance to the experimental setup. Due to the achieved purity of the secondary beam during the data collection run,

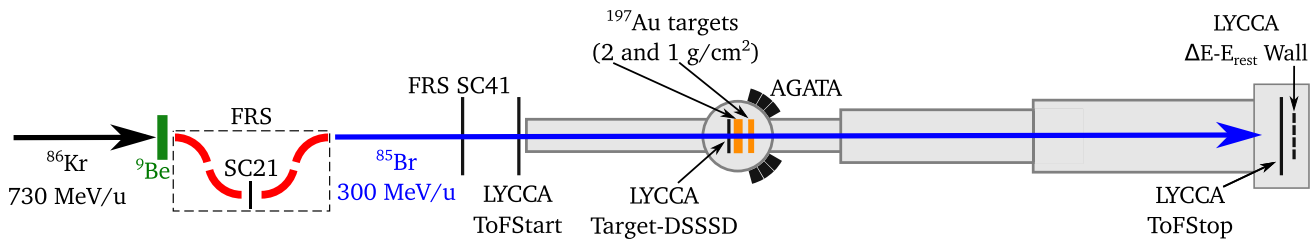


**Fig. 1** A schematic drawing of the experimental setup adapted from [21]. The incident  $^{86}\text{Kr}$  beam is depicted in black, the  $^9\text{Be}$  fragmentation target in green, and the secondary  $^{85}\text{Br}$  beam in blue. In addition, the FRS SC21 inside the FRS and the SC41 scintillator directly in front of the experimental hall as well as all LYCCA components present in

the experiments are depicted. The target chamber with the two gold targets (in orange) as well as AGATA is shown in the center. For simplicity reasons, the FRS is only schematically shown with its dipole magnets in red (for details see [10]). LYCCA’s ToFStart detector was not used in the analysis

all particle-tracking and energy-loss detectors of the FRS were switched off to reduce dead-time and increase the feasibility of the data acquisition at this rate. Time-of-flight scintillation detectors were operating. Outgoing particle identification, energy loss, total energy and velocity measurements were achieved via LYCCA. After impinging on the gold targets with thicknesses of  $2\text{ g/cm}^2$  and  $1\text{ g/cm}^2$ , respectively, the secondary  $^{85}\text{Br}$  beam had a kinetic energy of approximately  $242\text{ MeV/u}$  after the first and  $210\text{ MeV/u}$  after the second target calculated via LISE++<sup>1</sup>. This resulted in relative Doppler-shift differences  $\Delta E/E \approx 33\%$  under the assumption of a  $\gamma$  ray emitted at the first target corresponding to a polar angle of  $30^\circ$  with respect to the beam direction. The emission angle at the second target in respect to the same detection point would be  $47^\circ$ . Emitted  $\gamma$  rays were detected by AGATA. During the experiment, AGATA comprised 21 hexagonal 36-fold segmented HPGe detectors [18]. For particle identification of the outgoing beam, LYCCA’s  $\Delta E - E_{\text{rest}}$  wall was used [11]. Each wall module consisted of a double-sided silicon strip detector (DSSSD) used for energy-loss and position measurements with thicknesses in the range of  $300 - 320\ \mu\text{m}$  as well as nine CsI(Tl) scintillators for kinetic energy measurement with two possible thicknesses of  $33$  or  $10\text{ mm}$ . Since the energy loss is proportional to the charge  $Z^2$  of the incident particle and the total kinetic energy measurement is sensitive to the particles mass number  $A$ , the correlation between  $\Delta E$  and  $E_{\text{rest}}$  can be used to identify the incident nuclei (see [11] for details). In the experimental setup, a total of  $15\ \Delta E - E_{\text{rest}}$  wall modules were used. In addition, LYCCA’s Time-of-Flight (ToF) detectors were used. They consisted of two independent plastic scintillators in a circular shape with a diameter of  $270\text{ mm}$  and a thickness of  $1\text{ mm}$ . The light yield from the beam particle interaction with the scintillators was read out by 32 photomultiplier tubes [19]. One ToF detector was situated in front of the reaction chamber called ToFStart and another one was situated in front of the  $\Delta E - E_{\text{rest}}$  wall, called ToFStop. The ToF-

Stop detector was used to measure the beam-spot position via the method proposed in [20] in front of the  $\Delta E - E_{\text{rest}}$  wall modules. A schematic drawing of the experimental setup is shown in Fig. 1.

This first performance test of the *Coulex-multipolarimetry* was conducted with approximately three days of beam time. In the following, expected yields as well as necessary particle conditions for the benchmark test are presented.

### 3 Data analysis

#### 3.1 Expected relative yields

To estimate the performance of the *Coulex-multipolarimetry*, the  $\gamma$ -ray detection-efficiency weighted excitation ratios of target-like  $^{197}\text{Au}$  to beam-like  $^{85}\text{Br}$  excitations need to be calculated. The main contributor to the  $^{197}\text{Au}$  excitations is the  $3/2_{\text{g.s.}}^+ \rightarrow 7/2_1^+$  excitation with corresponding  $E_{\gamma,\text{Au}} = 547.5\text{ keV}$ . The fraction  $\eta^*$  of target- to beam-like excitations can be estimated using DWEIKO [22,23] via

$$\eta^* := \frac{\sigma_{\text{Au}}(E_b)}{\sigma_{\text{Br}}(E_b)} \tag{1}$$

with the kinetic energy of the incident  $^{85}\text{Br}$  beam,  $E_b$ , and the respective cross sections  $\sigma_i(E_b)$  as a function of  $E_b$ . To estimate the  $M1$  transition strength of the spin-flip excitation in  $^{85}\text{Br}$ , a transition of a proton from a  $j = 1/2$  to a  $j = 3/2$  state for  $\ell = 1$  is used, given by

$$\begin{aligned} B(M1, 1/2 \rightarrow 3/2) &= \frac{1}{2} |(3/2||M1||1/2)|^2 \\ &= \frac{1}{2\pi} (g_\ell^\pi - g_s^\pi)^2 \mu_N^2 \\ &= 3.34 \mu_N^2. \end{aligned} \tag{2}$$

Here,  $g_\ell^\pi = 1$  is the orbital  $g$ -factor of proton and  $g_s^\pi = 5.59$  its unquenched spin  $g$ -factor. In addition, a small  $E2$  contri-

<sup>1</sup> He-parameterization [17] for energy-loss calculations was used.

**Table 1** Excitation cross sections  $\sigma_i$  calculated via DWEIKO for gold target and bromine beam and their ratio  $\eta^*$  [see Eq. (1)] for two different beam energies  $E_b$  at their respective targets. In addition, the ratios

$E_b$ (MeV/u)	$\beta$	$\sigma_{\text{Au}}$ (mb)	$\sigma_{\text{Br}}$ (mb)	$\eta^*$	$\frac{\epsilon_{\gamma}(\text{Au})}{\epsilon_{\gamma}(\text{Br})}$	$\eta$
300	0.65	63.4	4.72	13.4	0.98	13.2
242	0.61	73.0	4.64	15.7	1.23	19.4

bution of  $B(E2, \downarrow) = 1$  W.u. is assumed, yielding an  $E2/M1$  multipole-mixing ratio of  $\delta = 0.026$  and a lifetime of approximately 10 fs. For the  $7/2_1^+ \rightarrow 3/2_{\text{g.s.}}^+$  transition in  $^{197}\text{Au}$ ,  $B(E2, \downarrow) = 33$  W.u. [24] is used. Nuclear excitations were neglected. With these assumptions, the calculated excitation cross sections and their respective  $\eta^*$  for the two different beam energies at the respective targets are given in Table 1. The  $\gamma$ -ray detection-efficiency weighted excitation ratios can be expressed via

$$\eta_i = \eta_i^* \cdot \frac{\epsilon_{\gamma,i}(\text{Au})}{\epsilon_{\gamma,i}(\text{Br})} \quad (3)$$

with the detection efficiency of incident  $^{197}\text{Au}$   $\gamma$  rays emitted from target  $i$

$$\epsilon_{\gamma,i}(\text{Au}) = \frac{N_{\text{abs,Au},i}}{N_{\text{tot}}}, \quad (4)$$

with  $N_{\text{abs,Au},i}$  as the amount of fully-absorbed  $^{197}\text{Au}$   $\gamma$  rays emitted from target  $i$  and  $N_{\text{tot}}$  as the total amount of emitted  $\gamma$  rays. No significant Doppler-broadening of  $^{197}\text{Au}$   $\gamma$  rays is assumed. The integrated detection efficiency for  $\gamma$  rays emitted by the  $^{85}\text{Br}$  beam nuclei with energy  $E_{\gamma,\text{Br}}$  at target  $i$

$$\overline{\epsilon}_{\gamma,i}(\text{Br}) = \int_{-1}^1 d \cos \Theta \frac{N(E'_{\gamma,\text{Br}} | \text{abs.}, i)}{N_{\text{tot}}}. \quad (5)$$

Here,  $\Theta$  is the angle of  $\gamma$  emission in the center-of-mass frame of the beam and the Doppler-shifted energy  $E'_{\gamma,\text{Br}} = E'_{\gamma,\text{Br}}(\cos \Theta, \beta)$ . The amount of Lorentz-transformed and Doppler-shifted  $\gamma$  rays with emission angle  $\Theta$  that were fully absorbed by AGATA is  $N(E'_{\gamma,\text{Br}} | \text{abs.}, i)$ . Since only ratios between efficiencies are of interest [see Eq. (3)], a *Geant4* simulation [25–27] using the AGATA simulation code [28] was used to extract AGATA's ratio of detection efficiencies. Together with the simulated relative efficiencies, the  $\gamma$ -ray detection-efficiency weighted excitation ratios are  $\eta_1 = 13.2$  and  $\eta_2 = 19.4$ , respectively (see Table 1).

### 3.2 Particle conditions

To reduce the amount of background radiation in the  $\gamma$ -ray spectrum measured by AGATA, multiple particle con-

of expected efficiencies are given by  $\epsilon_{\gamma}(\text{Au})/\overline{\epsilon}_{\gamma}(\text{Br})$  as well as the  $\gamma$ -ray detection-efficiency weighted excitation ratios  $\eta$ , given by Eq. (3)

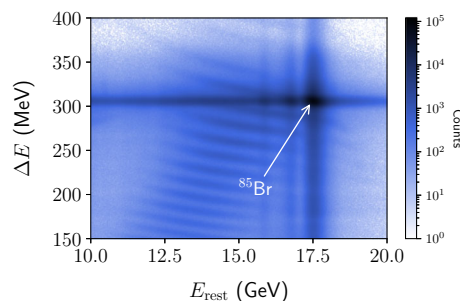


**Fig. 2** A two-dimensional spectrum of total remaining kinetic energy  $E_{\text{rest}}$  in the CsI(Tl) scintillators vs. energy loss  $\Delta E$  in the DSSSD of LYCCA's  $\Delta E$ - $E_{\text{rest}}$  wall modules. The peak at  $E_{\text{rest}} = 17.5$  GeV and  $\Delta E = 305$  MeV corresponds to  $^{85}\text{Br}$  nuclei. The diagonal lines correspond to various fragmentation products (see [11] for details)

ditions using LYCCA are applied. Particle identification can be achieved via a comparison of the energy loss  $\Delta E$  in the DSSSD and the measured total kinetic energy of the beam  $E_{\text{rest}}$  in the CsI(Tl) crystals, which is shown in Fig. 2. Only events with a particle multiplicity of one were analyzed since the assignment of energy-loss and total kinetic energy to identify an incident particle are not unambiguous for particle multiplicities larger than one. The multiplicity of one is assigned to a particle, if its particle multiplicity is equal to one both in the DSSSD and the CsI(Tl) detector wall. Roughly 33% of all events had a particle multiplicity of one. The two-dimensional  $E_{\text{rest}} - \Delta E$  spectrum (see Fig. 2) has been calibrated via LISE++ calculations based on the respective approximate energy losses of the  $^{85}\text{Br}$  beam after passing the second gold target. The peak at  $E_{\text{rest}} = 17.5$  GeV and  $\Delta E = 305$  MeV corresponds to  $^{85}\text{Br}$  nuclei. For  $15 \text{ GeV} < E_{\text{rest}} < 17.5 \text{ GeV}$  and  $\Delta E = 305 \text{ MeV}$ , additional peaks arise that very likely also correspond to  $^{85}\text{Br}$  nuclei. However, instabilities in the electronics most likely caused a wrong assignment of kinetic energy. In order to prevent a false identification of events that might not correspond to  $^{85}\text{Br}$ , these events were not included in the analysis. Hence, a reliable particle identification of LYCCA is limited to the peak at  $E_{\text{rest}} = 17.5(8) \text{ GeV}$  and  $\Delta E = 305(14) \text{ MeV}$  which contains 14% of all events. Most of the measured events were caused by light particles such as protons, neutrons or  $\gamma$  rays.

In addition, LYCCA's time-of-flight detector in front of the  $\Delta E - E_{\text{rest}}$  wall, can be used to pinpoint the correct travel path

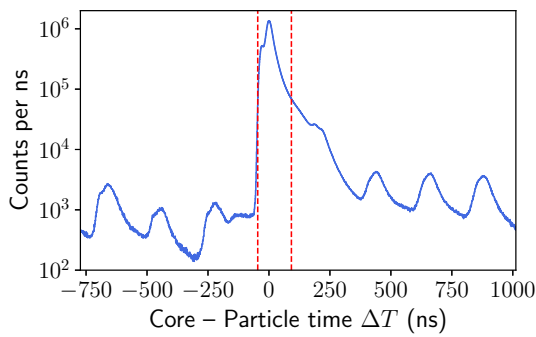


**Fig. 3** Time difference  $\Delta T$  between the particle time from FRS and AGATA’s time extracted via PSA in nanoseconds. All 21 AGATA crystal – FRS time differences have been offset to align at  $\Delta T = 0$  ns. The periodic structure is caused by the regular beam spills each 220 nanoseconds. The limits on  $\Delta T$  shown as red dashed lines select the prompt peak. It contains roughly 90% of all data

of the incident particles to avoid a false correlation of  $\Delta E$  and  $E_{rest}$ . This is achieved via a comparison of measured  $x$  and  $y$  values on the respective detectors, ToFStop, DSSSD and CsI(Tl). Ideally, their  $x$  and  $y$  values should perfectly align for a single particle traveling through all three detectors under the assumption that the beam impinges on the respective detector planes perpendicularly. Roughly 71% of all identified  $^{85}\text{Br}$  events were aligning with the ToFStop in their respective  $x$  and  $y$  values.

To access measured  $\gamma$  rays that are coincident to identified  $^{85}\text{Br}$  particles via LYCCA, the time difference between AGATA crystals and the FRS is used. This is achieved via the global trigger and synchronization system (GTS) timestamp which correlates AGATA’s data acquisition system (NARVAL) [12] to the GSI internal Multi Branch System (MBS) [29,30], to which the FRS is coupled. The difference  $\Delta T$  between the time of incident  $\gamma$  rays extracted from AGATA’s pulse shapes compared to the particle time measured by the FRS scintillator SC21 (see Fig. 1) is shown in Fig. 3.

#### 4 Results

The resulting  $\gamma$ -ray spectrum measured by AGATA for all 73 h of beam time is shown in Fig. 4. The total energy measured in the central contact in the respective AGATA crystals, referred to as cores, are depicted. Figure 4 shows all core energies in black without any condition on particle detectors and in blue with applied conditions as outlined in Sect. 3. The Doppler-corrected spectra for both targets are depicted in Fig. 5 with particle conditions applied. The interaction point with the largest deposited energy in the respective detector has been selected as the first interaction point of the incident  $\gamma$  ray. This point is used for calculating the angle between the beam direction and the emitted photon. The expected

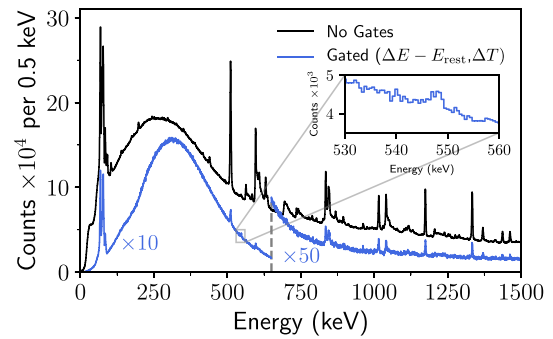


**Fig. 4** Core energies measured by AGATA in  $\sim 73$  h of beam time without conditions on any ancillary detectors in black and with  $^{85}\text{Br}$  particle identification condition on LYCCA and time condition on prompt beam in blue (see Sect. 3). For better visibility, the gated spectrum was upscaled by a factor of ten for energies up to 650 keV and by a factor of 50 for larger energies

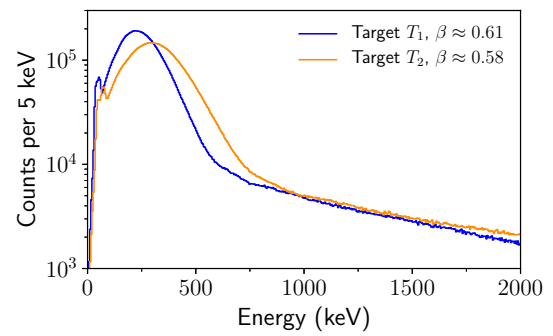


**Fig. 5** Doppler-corrected spectra for the respective velocities  $\beta$  after target 1 (blue) and target 2 (orange). Conditions as outlined in Sect. 3 are applied. No  $1/2^- \rightarrow 3/2^-_{g.s.}$  transitions of  $^{85}\text{Br}$  are noticeable

approximate beam velocities after the respective targets 1 and 2, defined as  $T_1$  and  $T_2$ , are  $\beta_1 \approx 0.61$  and  $\beta_2 \approx 0.58$  which were calculated via LISE++ calculations (similar to Sect. 3.1). These velocities are assumed as the beam velocity during emission of photons from potential excited states of beam-like ions at the respective targets.

As shown in Fig. 6 (top), the Coulomb excitation of the  $^{197}\text{Au}$  targets is present at 547.5 keV. In total,  $A_{Au} = 2110(370)$  counts could be measured after applying all mentioned particle conditions (see Sect. 3). Given the incident particle rate of  $4.9 \times 10^4 \text{ s}^{-1}$  and the Coulomb-excitation probability of the targets of  $3 \times 10^{-4}$ , calculated from the gold-excitation cross sections from DWEIKO together with the respective target thicknesses, the average rate of  $^{197}\text{Au}$  excitations is  $14.7 \text{ s}^{-1}$ . With a photo-absorption efficiency of AGATA of 3.7% at a  $\gamma$ -ray energy of 547.5 keV, all mentioned conditions on the detected particles on the  $\Delta E - E_{rest}$  wall together with ToFStop (see Sect. 3.2), the condition on the particle- $\gamma$  time  $\Delta T$  (see Fig. 3), an approximate geometrical efficiency of LYCCA of 88% (see [21] for details)

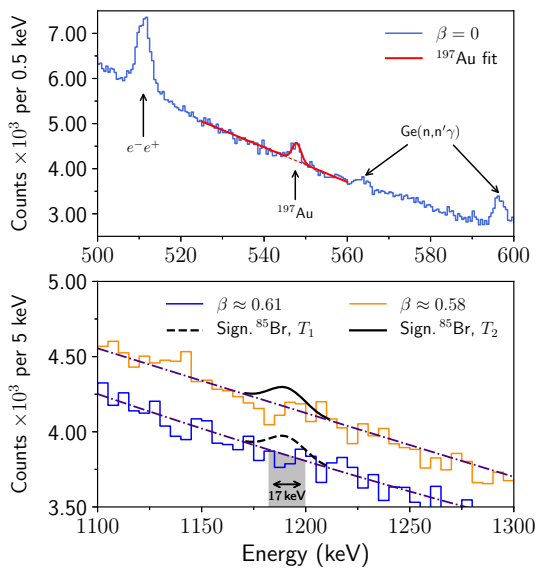


**Fig. 6** *Top*: Zoom into gated spectrum (no Doppler-corrections) from Fig. 4 around the  $^{197}\text{Au}$  Coulomb-excitation peak. A background subtracted fit on the  $^{197}\text{Au}$  peak is depicted (red). *Bottom*: Doppler-corrected spectra for  $T_1$  ( $\beta \approx 0.61$ ) and  $T_2$  ( $\beta \approx 0.58$ ) around the energy of the potential spin-flip transition in  $^{85}\text{Br}$ . Hypothetical statistical significant [see Eq. (7)]  $^{85}\text{Br}$  peaks at 1191 keV above the background radiation (approximated via a quadratic function; purple, dashed-dotted) are depicted for  $T_1$  (black, dashed) and  $T_2$  (black, solid). The integration window used for estimating the potential  $^{85}\text{Br}$  peak is shown in gray with width  $2\sigma_E = 17$  keV [see Eq. (6)]

and the mean alive-time ratio<sup>2</sup> of the setup of 55%, the amount of expected measurable  $\gamma$  rays from gold excitations is  $A_{\text{Au,exp.}} \approx 2030$ , agreeing with the measured value  $A_{\text{Au}} = 2110(370)$  within uncertainties. It is assumed that all measured  $^{197}\text{Au}$  excitations are caused by the identified  $^{85}\text{Br}$  beam particles.

Since the ratio of target to beam excitations can be calculated using the assumed  $M1$  and  $E2$  transition strengths (see Sect. 3.1) via DWEIKO, 160 counts for  $T_1$  and 110 counts for  $T_2$  in the Doppler-corrected spectra for the potential spin-flip transitions of  $^{85}\text{Br}$  are anticipated during the test experiment. As depicted in Figs. 5 and 6 (bottom panel), no  $1/2_1^- \rightarrow 3/2_{\text{g.s.}}^-$  transitions of  $^{85}\text{Br}$  beam particles are noticeable above background in the Doppler-corrected spectra.

Although the potential  $\pi p_{3/2} \rightarrow \pi p_{1/2}$  spin-flip transition in  $^{85}\text{Br}$  could not be resolved via the measured core energies, a detection limit can be estimated using the measured data.

### 5 Discussion

To calculate the detection limit for a potential  $\pi p_{3/2} \rightarrow \pi p_{1/2}$  excitation in  $^{85}\text{Br}$ , a regression via a second order polynomial  $p_{T_i}(E)$  to the Doppler-corrected spectra around the

<sup>2</sup> Ratio of measurable time in an arbitrary time window.

area of interest of the potential spin-flip transition in  $^{85}\text{Br}$  at 1191 keV is performed. A second-order polynomial is used to account for the slight quadratic behavior at the area of interest around 1191 keV (see Fig. 5). The regressions are illustrated in Fig. 6 (bottom). The detection limit for a potential peak can be estimated via the background area for the respective targets  $T_i$

$$A_{B,T_i} = \int_{E_{\gamma,\text{Br}} - \sigma_E}^{E_{\gamma,\text{Br}} + \sigma_E} dE p_{T_i}(E), \tag{6}$$

with  $\sigma_E = 8.5$  keV [ $\hat{=} 20$  keV full width at half maximum (FWHM)] as the width of the integration interval. Due to uncertainties arising during the Doppler-correction process, the peak width of the peak at 1191 keV is expected to be significantly broader than for  $\gamma$  rays emitted from nuclei at rest. In addition, the expected peak shape of the Doppler-corrected 1191 keV  $\gamma$  rays is complex, differing from a Gaussian distribution [8]. Assuming a Gaussian shape with a FWHM  $\approx 20$  keV, calculated via *Geant4* simulations, as an approximation, the minimum number of counts  $A_P$  necessary to identify a peak that is above the background level is approximately given by [31]

$$A_{P,T_i} = 4.65 \Delta A_{B,T_i} = 4.65 \sqrt{A_{B,T_i}}. \tag{7}$$

With  $A_{B,T_1} = 13060$  and  $A_{B,T_2} = 14140$ , the potential  $^{85}\text{Br}$  peak has to consist of at least 530 counts for  $T_1$  or 550 counts for  $T_2$  to be statistically significant. The statistically significant peaks are depicted in Fig. 6 (bottom). From the assumed ratio of  $^{85}\text{Br}$  to  $^{197}\text{Au}$  excitations, the minimal amount of necessary target excitations can be inferred (see Sect. 3.1). Given the ratio of  $\eta_1 = 13.2$  for  $T_1$  and  $\eta_2 = 19.4$  for  $T_2$ , a total of  $N_{\text{need},T_1} = 7000$  or  $N_{\text{need},T_2} = 10670$  detected respective target excitations would be necessary to be able to detect a significant amount of beam excitations (see Fig. 6). The ratio of necessary  $N_{\text{need},T_1}$  and  $N_{\text{need},T_2}$  to measured  $N_{\text{meas}}$  target excitations is

$$\xi := \frac{N_{\text{need}}}{N_{\text{meas}}} = \frac{\rho N_{\text{need},T_1} + (1-\rho) N_{\text{need},T_2}}{N_{\text{meas}}} = 4.3(8). \tag{8}$$

Here,

$$\rho = \frac{N_{T_1} \frac{\sigma_{\text{Br},T_1}}{\sigma_{\text{Br},T_2}}}{N_{T_1} + N_{T_2} \frac{\sigma_{\text{Br},T_1}}{\sigma_{\text{Br},T_2}}} = \frac{3.9 \times 10^5 \cdot 4.72 \text{ mb}}{(3.9 + 4.9) \times 10^5 \cdot 4.64 \text{ mb}} \approx 0.45 \tag{9}$$

is used as the ratio between the photo-absorption efficiency of  $^{85}\text{Br}$   $1/2_1^- \rightarrow 3/2_{\text{g.s.}}^-$  transition  $\gamma$  rays purely emitted from  $T_1$  compared to  $T_2$  scaled by their respective excitation cross sections  $\sigma_{\text{Br},T_i}$  (see Table 1). The different  $N_{T_i}$  have been calculated via a *Geant4* simulation with Doppler-shifted 1191 keV  $\gamma$  rays emitted either from  $T_1$  or  $T_2$  with respective

beam velocities  $\beta_1 \approx 0.61$  and  $\beta_2 \approx 0.58$ . In addition, the isotropically distributed angle of emission  $\Theta$  of the simulated  $\gamma$  rays in the center-of-mass frame of the beam is Lorentz-transformed via

$$\cos \vartheta = \frac{\cos \Theta + \beta_i}{1 + \beta_i \cos \Theta}, \quad i \in \{1, 2\} \tag{10}$$

where  $\vartheta$  is the angle of emission in the laboratory frame.

To get an estimate on the upper limit of the  $M1$  transition strength of the spin-flip excitation, the ratio

$$\kappa = \frac{A_{\text{Au}}}{\rho A_{\text{Bg},1} + (1 - \rho) A_{\text{Bg},2}} \tag{11}$$

between the measured  $^{197}\text{Au}$  excitations  $A_{\text{Au}}$  as well as the upper limit of a potential  $^{85}\text{Br}$  peak being indistinguishable from the background level within a 95 % confidence interval, given by [31]

$$A_{\text{Bg},i} = 2.33 \sqrt{A_{B,T_i}} \tag{12}$$

can be used, yielding  $\kappa = 7.8(14)$ . Since  $\kappa \approx \sigma_{\text{Au},T_i} / \sigma_{\text{Br},T_i}$  also holds, due to  $A_{\text{Au}}$  and  $A_{\text{Bg},i}$  being linked to the respective cross sections, the upper limit for the cross section of  $^{85}\text{Br}$  at  $T_2$  hence can be estimated via

$$\sigma_{\text{Br},T_2} < \frac{\sigma_{\text{Au},T_2}}{\kappa - \Delta\kappa} = 11.4 \text{ mb.} \tag{13}$$

Using DWEIKO, the  $M1$  transition strength has an upper limit at  $B(M1, \downarrow) < 9.5 \mu_N^2$ .  $T_2$  was used here since it results in a larger upper limit for the  $B(M1, \downarrow)$  value than  $T_1$ . A  $B(E2, \downarrow) = 1 \text{ W.u.}$  with resulting  $\delta = 0.015$  would still allow for the application of the *Coulex-multipolarime-try* for such a large  $B(M1, \downarrow)$  value.

Given the assumption made in Sect. 3.1, the amount of necessary beam time for the used setup can be estimated. Since the amount of measurable  $^{85}\text{Br}$  transitions are directly linked to the measurable  $^{197}\text{Au}$  transitions via  $\eta_i$ , it follows that

$$A_{\text{Br}} = \frac{A_{\text{Au}}}{\rho \eta_1 + (1 - \rho) \eta_2} = \varrho A_{\text{Au}}, \tag{14}$$

where  $\varrho$  is used to account for the different probabilities of target- to beam-like excitations (see Sect. 3.1). In addition, from Eq. (7) follows that

$$A_{\text{Br}} \geq 4.65 \left[ \rho \sqrt{A_{B,T_1}} + (1 - \rho) \sqrt{A_{B,T_2}} \right]. \tag{15}$$

To access the measurement time, all peak areas  $A_i(t)$  can be expressed in terms of a counting rate  $\dot{A}_i(t)$  via

$$A_i(t) = \dot{A}_i(t) t \approx \frac{A_{i,\text{meas}}}{t_{\text{meas}}} t, \tag{16}$$

where  $t$  is the time,  $t_{\text{meas}} = 73 \text{ h}$  the measurement time and  $A_{i,\text{meas}}$  the respective measured amount of counts (e.g.  $A_{\text{Au}}$ ). Using Eqs. (14–16), the necessary measurement time for the given assumptions on  $B(M1, \downarrow)$ ,  $B(E2, \downarrow)$  and the resulting  $\delta$  (see Sec. 3.1) is

$$\begin{aligned} t_{\text{need}} &= t_{\text{meas}} \frac{4.65^2 \left[ \rho \sqrt{A_{B,T_1}} + (1 - \rho) \sqrt{A_{B,T_2}} \right]^2}{\varrho^2 A_{\text{Au}}^2} \\ &= 1330(470) \text{ h.} \end{aligned} \tag{17}$$

Hence, a significant  $^{85}\text{Br}$  peak at an energy of 1191 keV should be achievable in  $\approx 55$  days of beam time, given that the made assumptions on the transition strengths in  $^{85}\text{Br}$  are correct. Accessing particle multiplicities larger than one, resulting in roughly twice the amount of analyzable statistics, could decrease the necessary beam time down to  $\approx 28$  days, still rendering a measurement within the given limits of 73 hours of beam time impossible.

The planned AGATA  $1\pi$  configuration [32] with 45 crystals will further reduce the required beam time significantly. The expected reduction can be extracted from a *Geant4* simulation. For comparison purposes, simulations were performed for both setups, AGATA@PreSPEC and AGATA  $1\pi$ . Using beam velocities of  $\beta_1 \approx 0.61$  and  $\beta_2 \approx 0.58$  to take the Doppler effects into account. Table 2 gives the ratio

$$\nu := \frac{N_{1\pi}}{N_{\text{PreSPEC}}} \tag{18}$$

of the photo-absorption events in AGATA  $1\pi$  ( $N_{1\pi}$ ) and PreSPEC ( $N_{\text{PreSPEC}}$ ). Hence, an increase in statistics by a factor  $\nu \in [2.70, 2.83]$  is anticipated, yielding a necessary beam time of  $\approx 20$  days, if AGATA  $1\pi$  is used for the  $^{85}\text{Br}$  experiment, under the condition that only events with a particle multiplicity of one are used.

Up to this point, only total energy depositions in the full respective crystals were used. However, one of AGATA’s main features is the  $\gamma$ -ray tracking. Its impact on the analysis process is emphasized in the following.

### 6 Impact of $\gamma$ -ray Tracking

Since AGATA is a  $\gamma$ -ray tracking spectrometer, the performed peak analysis of  $^{197}\text{Au}$  (see Sects. 4 and 5) can also be

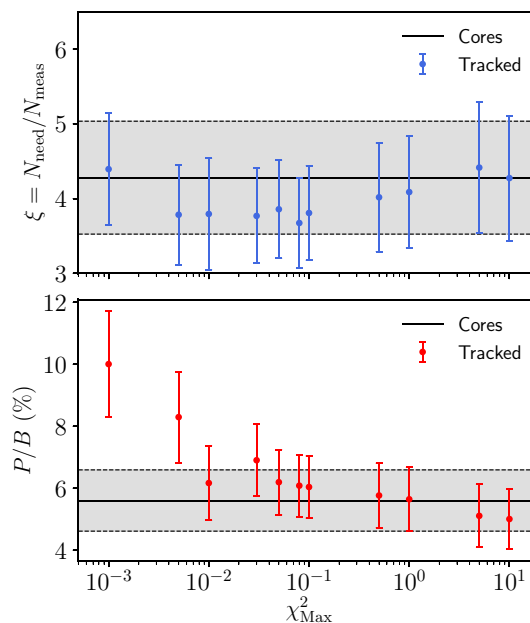
**Table 2** Expected increase of measurable  $^{85}\text{Br}$  excitations  $\nu$  with AGATA  $1\pi$ . Here,  $N_{1\pi}$  are the number of photo-absorbed  $\gamma$  rays with an energy of 1191 keV (Doppler-shifted and Lorentz-boosted) in the AGATA  $1\pi$  setup and  $N_{\text{PreSPEC}}$  respectively in the PreSPEC setup of AGATA

Target	$N_{1\pi}$	$N_{\text{PreSPEC}}$	$\nu$
$T_1$ (@ 0 cm)	$1.05 \times 10^6$	$3.9 \times 10^5$	2.70
$T_2$ (@ 10 cm)	$1.38 \times 10^6$	$4.9 \times 10^5$	2.83

done utilizing  $\gamma$ -ray tracked photons. To increase the selectivity of the used *Mars Gamma-ray Tracking* MGT [33–35], the  $\chi^2$  limit for accepted photons, referred to as  $\chi_{\text{Max}}^2$ , has to be chosen such that the best ratio  $\xi$  [see Eq. (8)] can be achieved. The acceptance limit  $\chi_{\text{Max}}^2$  is used to compare measured energies  $E_{\text{dep},i}$  at the respective interaction points  $\mathbf{x}$  with their expected deposited energies stemming from geometrical angles between consecutive interaction points  $\mathbf{x}_i$  calculated via the Compton-scattering formula. Larger values of  $\chi_{\text{Max}}^2$  yield clusters of interaction points being often accepted as stemming from a single  $\gamma$  ray since even large discrepancies between assumed deposited energies from position measurement compared to actually measured deposited energies are accepted. This can lead to false reconstructions of  $\gamma$  rays, reducing the achievable Peak-to-Background ( $P/B$ ) ratios. Here,  $P/B$  is defined as the number of counts in a peak-of-interest above the fitted background level divided by the number of counts in the same range in the background<sup>3</sup>. The smaller  $\chi_{\text{Max}}^2$ , the larger the rejection of potentially false, but also correct clusters. For details on  $\gamma$ -ray tracking, see [33–36].

Following the approach given in Sects. 4 and 5, the  $\gamma$ -ray tracking with the mentioned acceptance limit of  $\chi_{\text{Max}}^2 = 0.08$  ultimately yielded the smallest  $\xi = 3.7(6)$  [see Eq. (8)] as depicted in Fig. 7. Although  $\chi_{\text{Max}}^2 = 10^{-3}$  resulted in a larger  $P/B = 10.0(17)\%$ , the amount of measured counts in the  $^{197}\text{Au}$  is 1050(180), roughly half as many events as measured in the core analysis (see Sect. 3). Since the amount of measured events in the Doppler-corrected background spectra are not as strongly suppressed, especially due to larger uncertainties in energy measurement as well as uncertainties arising in the Doppler-correction<sup>4</sup>, the resulting  $\xi = 4.4(7)$  for  $\chi_{\text{Max}}^2 = 10^{-3}$  is even larger than for the core analysis.

As shown in Fig. 8 for  $\chi_{\text{Max}}^2 = 0.08$ ,  $\gamma$ -ray tracking reduces the overall statistics severely but also suppresses unwanted background lines such as  $e^-e^+$  annihilation events or  $\text{Ge}(n,n'\gamma)$  reactions. Photons that do not stem from the defined source positions are suppressed via  $\gamma$ -ray tracking methods since their hypothetical traveling path through the detector, assumed to start from the source position, can strongly differ from their physical path. Applying  $\gamma$ -ray

**Fig. 7** *Top*: Detection limit ratios  $\xi$  for various  $\chi_{\text{Max}}^2$  parameters of MGT (blue). The black line corresponds to core energies (see Sects. 4 and 5) with respective uncertainties as dashed lines. *Bottom*: Peak-to-Background ( $P/B$ ) ratios for tracked  $\gamma$  rays as a function of  $\chi_{\text{Max}}^2$ . The highest  $P/B$  ratio can be achieved for the lowest  $\chi_{\text{Max}}^2 = 10^{-3}$ . However, the achieved  $\xi$  is not optimal in this scenario

tracking, the background level in the Doppler-corrected spectra also decreases significantly. Comparing the  $P/B$  ratios of the  $^{197}\text{Au}$  peak for tracked  $\gamma$  rays and core energies, a  $P/B_{\text{core}} = 5.6(9)\%$  for the core energies and a  $P/B_{\text{track}} = 6.1(10)\%$  for the tracked  $\gamma$  rays could be achieved. Under the assumption that AGATA  $1\pi$  is available,  $\gamma$ -ray tracking could reduce the necessary beam time to  $\approx 15$  days, under the condition that only events with a particle multiplicity of one are used.

Depending on the assumed  $B(M1, \downarrow)$  value, the necessary measurement time  $t_{\text{need}}$  varies strongly (see Fig. 9). For example, if a similar  $B(M1, \downarrow)$  value as measured in  $^{87}\text{Rb}$  is assumed,  $t_{\text{need}} \approx 170$  d, an impractical amount of beam time. However, it is likely that a future experiment will be performed using, e.g., the Super-FRS [37], the successor of FRS at the Facility for Antiproton- and Ion-Research (FAIR). Since light particles such as protons or neutrons are the main cause for the present background, a sufficient reduction of these events achievable with the Super-FRS will most likely

<sup>3</sup> A  $2\sigma$  interval around the peak-of-interest was used for the  $P/B$  calculations.

<sup>4</sup> Point of  $\gamma$ -ray emission not perfectly known.

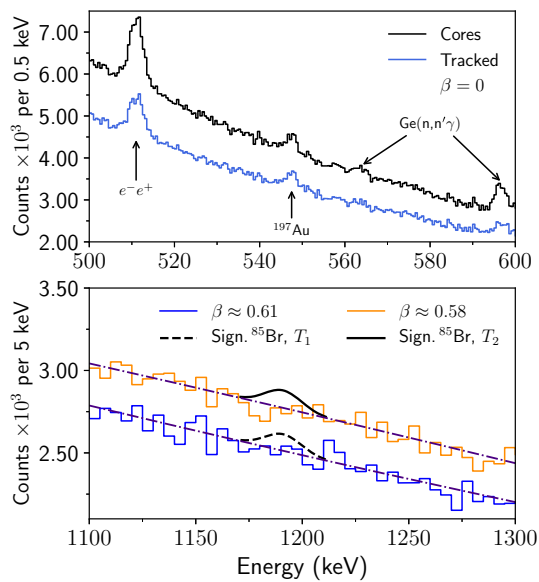


**Fig. 8** *Top*: Tracked photon energies with applied particle conditions for  $\chi^2_{\text{Max}} = 0.08$  (blue) and core energies (black). Although the overall statistics are reduced, events in the “tracked” histograms do not (necessarily) stem from the target position such as Ge(n,n’ $\gamma$ ) reactions at around 596 keV as well as  $e^-e^+$  annihilation photons at 511 keV are suppressed in comparison to the core spectrum. *Bottom*: Doppler-corrected spectra for tracked photons for  $T_1$  and  $T_2$  with their respective significant  $^{85}\text{Br}$  peaks

cause a strong reduction of background events. The impact of background reduction at the site of the experiment is shown in Fig. 9. Assuming that the general background level is decreased by an order of magnitude if the Super-FRS is used, the necessary measurement time would be reduced by that same factor, allowing a measurement of the  $\pi p_{3/2} \rightarrow \pi p_{1/2}$  spin-flip in  $^{85}\text{Br}$  for  $B(M1, \downarrow) = 0.64 \mu_N^2$  as measured in  $^{87}\text{Rb}$  in a similar time as achieved using the FRS for  $B(M1, \downarrow) = 3.34 \mu_N^2$ , corresponding to a proton spin-flip transition with an unquenched spin  $g$ -factor.

### 7 Conclusion and outlook

A first benchmark test of the *Coulex-multipolarimetry* method specifically developed for single-particle spin-flip experiments with AGATA via the expected  $\pi p_{3/2} \rightarrow \pi p_{1/2}$  spin-flip excitation in  $^{85}\text{Br}$  has been performed. In this experiment, a setup of two consecutive gold targets was used to measure target specific photon yields from  $^{85}\text{Br}$  beam-excitations which should provide information about the  $M1$  transition strength of the potential single-particle excitation. Although no de-excitations of the  $^{85}\text{Br}$  beam particles were observed, background levels together with the measured amount of gold target excitations could be used to infer an upper limit of the  $M1$  transition strength of  $B(M1, \downarrow) < 9.5 \mu_N^2$  as well as the necessary amount of addi-

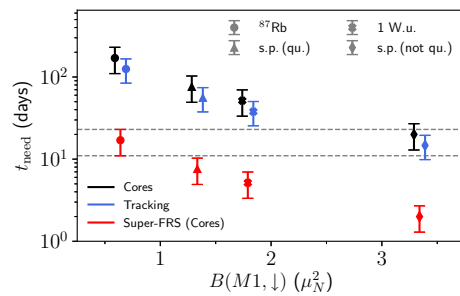


**Fig. 9** Necessary measurement time  $t_{\text{need}}$  with AGATA  $1\pi$  as a function of expected  $B(M1, \downarrow)$  for a transition strength as measured in  $^{87}\text{Rb}$  (dots at  $0.64 \mu_N^2$ ), 1 W.u. (crosses at  $1.75 \mu_N^2$ ), a single particle transition with quenched  $g_s^\pi$  (triangles at  $1.33 \mu_N^2$ ) and without a quenched  $g_s^\pi$  (diamonds at  $3.34 \mu_N^2$ ). Points in black depict the necessary time when core energies are used, blue if  $\gamma$ -ray tracking is used and red, if the Super-FRS is used as a fragment separator. Here, it is assumed that for a constant signal, the background is reduced by an order of magnitude compared to the present data set obtained using the FRS. Only the case where cores are used is depicted for this hypothetical case. A significant  $^{85}\text{Br}$  peak could be measured using the Super-FRS for a  $B(M1, \downarrow) = 0.64 \mu_N^2$  in a similar time as it would be measured using the FRS for  $B(M1, \downarrow) = 3.34 \mu_N^2$

tional beam time of  $\approx 55$  days for the setup employed here. Via *Geant4* simulations of AGATA, the impact of the upcoming AGATA  $1\pi$  configuration has been studied. Together with AGATA’s  $\gamma$ -ray tracking capabilities, the amount of beam time using AGATA in its  $1\pi$  configuration would be reduced by a factor of three. Further significant reduction of necessary beam time can be expected due to the anticipated decrease in beam-related background radiation at the HISPEC [38] site of the AGATA spectrometer. Hence, the experiment reported on here has served for identifying and establishing the limits of the available detector infrastructure at GSI in order to prepare for future experiments at HISPEC.

**Acknowledgements** The authors want to thank A. Lopez-Martens for helpful advice on possible analysis methods and U. Friman-Gayer for statistics-related advice. In addition, the authors want to thank the AGATA collaboration for providing the necessary data. This work was supported by the German BMBF under Grant Numbers 05P19RDFN1, 05P18RDFN9 and 05P19PKFNA, the Bulgarian National Science fund under grant number DN 08/23, the Swedish Research Council under contracts Nos. 2010-147, 2011-5253 and 2011-6127, HGS-HIRE and HIC for FAIR. This work has been supported by the European Community FP7–Capacities, ENSAR Contract No. 262010.

**Data Availability Statement** This manuscript has no associated data or the data will not be deposited. [Authors’ comment: The datasets generated during and/or analysed during the current study are available from the corresponding author on reasonable request.]

### References

1. R. Taniuchi et al.,  $^{78}\text{Ni}$  revealed as a doubly magic stronghold against nuclear deformation. *Nature* **569**, 53 (2019)

2. S. Franchoo et al., Beta Decay of  $^{68-74}\text{Ni}$  and level structure of Neutron-Rich Cu isotopes. *Phys. Rev. Lett.* **81**, 3100 (1998)
3. S. Franchoo et al., Monopole migration in  $^{69,71,73}\text{Cu}$  observed from  $\beta$  decay of laser-ionized  $^{68-74}\text{Ni}$ . *Phys. Rev. C* **64**, 054308 (2001)
4. K.T. Flanagan et al., Nuclear spins and magnetic moments of  $^{71,73,75}\text{Cu}$ : inversion of  $\pi 1p_{3/2}$  and  $\pi 1f_{5/2}$  levels in  $^{75}\text{Cu}$ . *Phys. Rev. Lett.* **103**, 142501 (2009)
5. T. Otsuka et al., Evolution of nuclear shells due to the tensor force. *Phys. Rev. Lett.* **95**, 232502 (2005)
6. T. Otsuka et al., Novel features of nuclear forces and shell evolution in exotic nuclei. *Phys. Rev. Lett.* **104**, 012501 (2010)
7. C. Stahl et al., Identification of the proton  $2p_{1/2} \rightarrow 2p_{3/2}$  M1 spin-flip transition in  $^{87}\text{Rb}$ . *Phys. Rev. C* **87**, 037302 (2013)
8. C. Stahl et al., Coulex-multipolarimetry with relativistic heavy-ion beams. *Nucl. Instrum. Methods Phys. Res. A* **770**, 123 (2015)
9. N. Pietralla et al., On the road to FAIR: 1<sup>st</sup>. Operation of AGATA in PreSPEC at GSI, EPJ Web of Conferences 66, 02083 (2014)
10. H. Geissel et al., The GSI projectile fragment separator (FRS): a versatile magnetic system for relativistic heavy ions. *Nucl. Instrum. Methods Phys. Res. Sect. B* **70**, 14 (1992)
11. P. Golubev et al., The Lund–York–Cologne Calorimeter (LYCCA): concept, design and prototype developments for a FAIR-NUSTAR detector system to discriminate relativistic heavy-ion reaction products. *Nucl. Instrum. Methods Phys. Res. Sect. A* **723**, 55 (2013)
12. A. Akkoyun et al., AGATA-Advanced gamma tracking array. *Nucl. Instrum. Methods Phys. Res. A* **668**, 26 (2012)
13. A. Maj et al., Angular distribution of photons from the decay of the GDR in hot and rotating light Yb nuclei from exclusive experiments. *Nucl. Phys. A* **571**, 185 (1994)
14. A. Winther, K. Alder, Relativistic coulomb excitation. *Nucl. Phys. A* **319**, 518 (1979)
15. J. Lindhard, A.H. Sørensen, Relativistic theory of stopping for heavy ions. *Phys. Rev. A* **53**, 2443 (1996)
16. O. Tarasov, D. Bazin, LISE++: radioactive beam production with in-flight separators. *Nucl. Instrum. Methods Phys. Res. B* **266**, 4657 (2008)
17. F. Hubert et al., Range and stopping-power tables for 2.5–500 MeV/nucleon heavy ions in solids, *Atomic Data and Nuclear Data* 46, 1 (1990)
18. N. Lalović et al., Performance of the AGATA  $\gamma$ -ray spectrometer in the PreSPEC set-up at GSI. *Nucl. Instrum. Methods Phys. Res. A* **806**, 258 (2016)
19. R. Hoischen et al., Fast timing with plastic scintillators for in-beam heavy-ion spectroscopy. *Nucl. Instrum. Methods Phys. Res. A* **654**, 354 (2011)
20. M. Reese et al., Position sensitivity of LYCCA time-of-flight detectors. *GSI Rep.* **2013–1**, 185 (2013)
21. M. Reese, Intermediate-energy Coulomb excitation with the PreSPEC-AGATA setup, Ph.D. thesis, Technische Universität Darmstadt, (2018)
22. C. Bertulani, A computer program for relativistic multiple Coulomb and nuclear excitation. *Comput. Phys. Commun.* **116**, 23 (1999)
23. C. Bertulani, DWEIKO, [http://cpc.cs.qub.ac.uk/summaries/ADRN\\_v1\\_0.html](http://cpc.cs.qub.ac.uk/summaries/ADRN_v1_0.html). Accessed 21 Oct 2019
24. A.E. Stuchbery et al., Measured gyromagnetic ratios and the low-excitation spectroscopy of  $^{197}\text{Au}$ . *Nucl. Phys. A* **486**, 374 (1988)
25. S. Agostinelli et al., Geant4 – a simulation toolkit. *Nucl. Instrum. Methods Phys. Res. A* **506**, 250 (2003)
26. J. Allison et al., Geant4 developments and applications. *IEEE Trans. Nucl. Sci.* **53**, 270 (2006)
27. J. Allison et al., Recent developments in GEANT4. *Nucl. Instrum. Methods Phys. Res. A* **835**, 186 (2016)
28. E. Farnea et al., Conceptual design and Monte Carlo simulations of the AGATA array. *Nucl. Instrum. Methods Phys. Res. A* **621**, 331 (2010)
29. H. Essel, N. Kurz, The general purpose data acquisition system MBS, 1999 IEEE Conference on Real-Time Computer Applications in Nuclear Particle and Plasma Physics 475, (1999)
30. H. Essel et al., The new data acquisition system at GSI. *IEEE Trans. Nucl. Sci.* **43**, 1 (1996)
31. G.F. Knoll, *Radiation detection and measurement*, vol. 4 (Wiley, New York, 2010)
32. E. Clément, Conceptual design of the AGATA  $1\pi$  array at GANIL. *Nucl. Instrum. Methods Phys. Res. A* **855**, 1 (2017)
33. D. Bazzacco, *Nucl. Phys. A* **746**, 248 (2004). (Proceedings of the 2029 Sixth International Conference on Radioactive Nuclear Beams (RNB6))
34. R.M. Lieder et al., The TMR network project “Development of  $\gamma$ -ray tracking detectors”. *Nucl. Phys. A* **682**, 279c (2001)
35. A. Korichi, T. Lauritsen, Tracking  $\gamma$  rays in highly segmented HPGe detectors: a review of AGATA and GRETINA. *Eur. Phys. J. A* **55**, 121 (2019)
36. A. Lopez-Martens et al.,  $\gamma$ -ray tracking algorithms: a comparison. *Nucl. Instrum. Methods Phys. Res. A* **533**, 454 (2004)
37. H. Geissel et al., *Technical design report on the super-FRS. Technical report* (GSI, Darmstadt, 2009)
38. Zs. Podolyák, The high-resolution in-flight spectroscopy (HISPEC) project at FAIR. *Int. J. Mod. Phys. E* **15**, 1967 (2006)